1 **Near-native state imaging by cryo-soft-X-ray tomography reveals remodelling of cytoplasmic**

2 **vesicles and mitochondria during HSV-1 infection**

3

4 Kamal L. Nahas[1,2], Viv Connor[1], Maria Harkiolaki[2]*, Colin M. Crump[1]*, Stephen C. Graham[1]*

5 [1]Department of Pathology, University of Cambridge, Tennis Court Road, Cambridge CB2 1QP, United

6 Kingdom.

7 [2] Beamline B24, Diamond Light Source, Harwell Science and Innovation Campus, Didcot OX11 0DE,

8 United Kingdom.

9 *Corresponding authors: Maria Harkiolaki, maria.harkiolaki@diamond.ac.uk; Colin M. Crump,

10 cmc56@cam.ac.uk; Stephen C. Graham, scg34@cam.ac.uk

11 **ORCIDs:** KLN 0000-0003-3501-8473; CMC 0000-0001-9918-9998; SCG 0000-0003-4547-4034; MH

12 0000-0001-8091-9057

17 **Short Title:** Cryo-soft-X-ray tomography of HSV-1 infection

19

20   **Abstract**

21   Herpes simplex virus-1 (HSV-1) is a large, enveloped DNA virus and its assembly in the cell is a

22   complex multi-step process during which viral particles interact with numerous cellular compartments

23   such as the nucleus and organelles of the secretory pathway. Transmission electron microscopy and

24   fluorescence microscopy are commonly used to study HSV-1 infection. However, 2D imaging limits our

25   understanding of the 3D geometric changes to cellular compartments that accompany infection and

26   sample processing can introduce morphological artefacts that complicate interpretation. In this study,

27   we used a 3D imaging technique (soft X-ray tomography) to observe differences in whole-cell

28   architecture between HSV-1 infected and uninfected cells. To protect the near-native structure of

29   cellular compartments, we used a non-disruptive sample preparation technique involving rapid

30   cryopreservation. We observed viral capsids and assembly intermediates interacting with nuclear and

31   cytoplasmic membranes. Furthermore, we observed differences in the morphology of specific

32   organelles between uninfected and infected cells. The local concentration of cytoplasmic vesicles at

33   the juxtanuclear compartment increased and their mean width decreased as infection proceeded.

34   Furthermore, mitochondria in infected cells were elongated and highly branched, suggesting that

35   altered dynamics of mitochondrial fission/fusion accompany HSV-1 infection. Our results demonstrate

36   that high-resolution 3D images of cellular compartments can be captured in a near-native state using

37   soft X-ray tomography and have revealed that infection causes striking changes to the morphology of

38   intracellular organelles.

39

40

41 **Importance**

42 Ultrastructural changes to the morphology and organization of cellular compartments during herpes

43 simplex virus-1 (HSV-1) infection have not been studied under near-physiological conditions. In this

44 study, near-native state X-ray imaging was used to image the ultrastructure of HSV-1 and cellular

45 compartments during infection, identifying striking changes to the abundance and organization of

46 cytoplasmic vesicles and mitochondria. The concentration of vesicles in the juxtanuclear region

47 increased with time post infection, which could represent an increasing supply of vesicles to support

48 capsid envelopment. Mitochondria are dynamic cellular compartments that undergo fusion to share

49 resources and fission followed by mitophagy to recycle damaged components. Here we show that

50 mitochondria tend to elongate and form highly-branched networks as infection progresses, suggesting

51 fusion predominates over fission during HSV-1 infection. These findings offer insight into stages of virion

52 morphogenesis and the cellular response to infection.

53

54

Introduction

Herpes simplex virus-1 (HSV-1) is a large, enveloped DNA virus in the *Alphaherpesvirinae* subfamily of *Herpesviridae* that establishes a persistent life-long latent infection in sensory and sympathetic neurons, occasionally reactivating to cause lytic replication in oral or genital mucosal epithelial cells that culminates in cold sores and genital herpes, respectively[1]. The production of viral particles during lytic replication is a complex process involving multiple cellular compartments[2–6].

In the first step of virion morphogenesis, capsid assembly and genome packaging occur in the nucleus[7]. Fully formed nucleocapsids must cross the nuclear envelope to migrate into the cytoplasm and undergo latter stages of virus assembly – a process which involves close interaction between nucleocapsids and the membranes of the nuclear envelope. Unlike individual proteins, the nucleocapsids are too large to pass through nuclear pores and must therefore first bud into the perinuclear space through the inner-nuclear membrane, forming a perinuclear viral particle (primary envelopment). The envelope of this particle subsequently fuses with the outer-nuclear membrane to release the nucleocapsid into the cytoplasm (de-envelopment)[8–11]. Numerous copies of multiple (≥ 23) viral proteins deposit on the surface of nucleocapsids in the nucleus and cytoplasm to form an amorphous proteinaceous layer known as the tegument[12]. Tegument proteins have multiple important roles during infection, including the promotion of virion maturation[2,3,6]. Several cytoplasmic compartments are essential to virion morphogenesis: viral proteins are synthesized and modified in the endoplasmic reticulum and Golgi complex and, in a process known as secondary envelopment, nucleocapsids acquire their membrane envelope from cytoplasmic vesicles that are thought to be derived from the *trans*-Golgi network and the endosomal system[2,3,13]. In addition to compartments directly involved in virion assembly, the cytoskeleton and other cellular organelles, such as mitochondria and lysosomes, can become remodelled in response to infection[14–16]. Understanding how the morphology and organization of cellular compartments change during infection could illuminate their involvement in virion morphogenesis and in the cellular response to HSV-1 infection.

Previous studies to characterize remodelling of cellular compartments have identified numerous changes that accompany HSV-1 infection, including the fragmentation of the Golgi complex and the condensation of the endoplasmic reticulum around the nuclear rim[17,18]. A more comprehensive study has recently been carried out using a recombinant form of HSV-1, known as the "timestamp" reporter

4

84   virus, expressing fluorescent chimeras of the early protein ICP0 and the late protein gC to distinguish

85   between early and late stages of infection[16]. Eight cellular compartments were compared between

86   uninfected and timestamp virus-infected human TERT-immortalized human foreskin fibroblast (HFF-

87   hTERT) cells, with high-resolution spatial data collected using structured illumination microscopy (SIM)

88   and expansion microscopy. Numerous changes in the morphology of cellular compartments were

89   observed as infection progressed, such as fragmentation of the Golgi complex at late stages of infection,

90   concentration of endosomes and lysosomes at a juxtanuclear compartment, and elongation of

91   mitochondria[16]. However, the extent to which sample preparation strategies may damage the

92   morphology of cellular structures remains poorly understood and it is possible that disruptive techniques

93   such as immunostaining or sample expansion could introduce artefacts in cellular ultrastructure[19–21].

94   Moreover, it is not clear if these changes to cellular compartments are consistent across different cell

95   types used to study HSV-1 infection.

96   In this study, we investigated changes to cellular compartments during infection with the HSV-1

97   timestamp reporter virus using soft X-ray tomography of cryopreserved samples (cryoSXT). Soft X-rays

98   used for this analysis have a lower energy (~500 eV)[22] and longer wavelength than the "hard" X rays

99   typically used for medical imaging (~15-30 keV)[23] or X-ray crystallography (~6–20 keV)[24]. The

100   wavelengths of soft X-rays used for cryoSXT are in the "water window" where structured carbon-rich

101   structures in the cell such as membranes produce considerable contrast whereas oxygen-rich

102   structures such as the "watery" cytosol remain transparent, thereby enabling cellular compartments to

103   be observed[22]. We used this label-free technique to image the ultrastructure of infected (and control)

104   cells, monitoring the 3D geometry and organization of cellular compartments[25]. The ultrastructure of the

105   samples was protected in a near-native state using a non-disruptive cryopreservation protocol[26]. Our

106   study focused on the ultrastructural changes that accompany HSV-1 infection of human osteosarcoma

107   U2OS cells, allowing comparison with previous reports from infection of HFF-hTERT cells[16]. Although

108   a few differences were observed between the extent of Golgi fragmentation and the subcellular

109   distribution of ICP0, we determined that remodelling of cytoplasmic vesicles and mitochondria was

110   largely similar between these cultured cells. Furthermore, the high resolution afforded by cryoSXT

111   revealed that mitochondria become highly branched during HSV-1 infection.

112

5

113 **Results**

114 *HSV-1 viral particles and assembly intermediates are detectable by cryoSXT*

115 While cryoSXT has been used to image virus particles in infected cells[25,27], it was unclear whether

116 'naked' HSV-1 capsids, which are approximately 125 nm in diameter[28,29], would be large enough and

117 offer sufficient contrast to be observed with this imaging method. To establish a baseline, we grew

118 uninfected HFF-hTERT cells on holey-carbon electron microscopy (EM) grids and plunge cryocooled

119 them for imaging by cryoSXT. Unlike a glass lens that focuses light by refraction, a zone plate was used

120 to focus the X rays by diffraction: a zone plate is a diffraction grating composed of a series of concentric

121 rings in which alternating rings are transparent to X rays and the resolution is determined by the

122 diameter of the outermost ring[30]. 25 nm zone plates, affording up to 30 nm resolution, were used for

123 our experiments here. To produce a tomogram, a series of X-ray projection images were collected from

124 a single 9.46×9.46 µm field of view in the cell, with each projection collected following rotation of the

125 specimen around an axis normal to the incident X-ray beam (tilt series). For each tomogram the

126 projections spanned up to 120° of rotation with increments of 0.2° or 0.5° per image. To correct for

127 vibrations in the microscope during imaging, the projections in the series were aligned together in the

128 program IMOD[31] using gold fiducials or lipid droplets as landmarks for registration. We collected 19 tilt

129 series that were processed into 3D tomograms and we found that the content of nuclei in uninfected

130 cells appear relatively featureless (**Fig 1A**).

131 Given that the nucleus is the site of capsid assembly, we sought to determine whether an abundance

132 of capsids could be detected in infected cells. To this end, HFF-hTERT cells were cultured on holey-

133 carbon EM grids, infected with 2 plaque-forming units (PFU) per cell of HSV-1 and plunge frozen at 16

134 hours post-infection (hpi). Infected cells were imaged via cryoSXT using a 40 nm zone plate objective

135 (**Fig. 1B**), illuminating a 15.14×15.14 µm field of view, using the image acquisition and analysis workflow

136 detailed above. These samples were prepared and cryopreserved on three different occasions and 98

137 tomograms were collected in total. Numerous dark puncta were observed in the nucleus of infected

138 cells (**Fig. 1C**). We interpreted these puncta to be HSV-1 capsids because capsids are rich in carbon

139 and phosphorous, being proteinaceous shells surrounding tightly packed DNA genomes, and these

140 elements exhibit strong absorption at the 500 eV X-ray energy used here for imaging[22]. During virus

141 assembly, capsids enter the perinuclear space by budding at the inner nuclear membrane (primary

6

142   envelopment), forming a membrane-wrapped perinuclear viral particle that rapidly fuses with the outer

143   nuclear membrane *en route* to the cytoplasm[9]. These enveloped virions in the perinuclear space are

144   infrequently observed by EM because they are short-lived and the thin sectioning required for imaging

145   using electron light decreases the probability that such structures will be present within the cellular

146   volume being examined. The high penetrating power of soft X-rays in unstained cryopreserved samples

147   (> 10 μm) removes the requirement for sectioning, allowing the entire depth of the cell to be imaged

148   simultaneously for any given field of view. This increases the likelihood of observing short-lived

149   structures such as primary enveloped viral particles. Dark puncta within the nuclear envelope that are

150   likely to be perinuclear viral particles were found 11 times in 98 tomograms (**Fig. 1D**). The perinuclear

151   viral particles appear to expand the perinuclear space and distend the nuclear envelope, as shown in

152   a segmented image (**Fig. 1E**). The width of the nuclear envelope at putative sites of primary

153   envelopment (190.6 ± 6.01 nm SEM; N=11) is significantly greater than the width of the nuclear

154   envelope in other places on the same tomograms (99.8 ± 3.57 nm SEM; N=11; paired t-test p-

155   value=$1.93×10^{-9}$) (**Fig. 1F**). This demonstrates the substantial deformation of the nuclear envelope that

156   must occur to accommodate perinuclear viral particles. Viral capsids were also observed in the

157   cytoplasm in close proximity to vesicles that are likely sites of secondary envelopment (**Fig. 1G**). After

158   secretion, HSV-1 particles commonly remain bound to the cell surface, a property that may be

159   exacerbated by the antiviral restriction factor tetherin[32,33]. In addition, we expected to see HSV-1

160   particles between cells because virions are targeted to cell junctions to promote cell-cell spread[34].

161   Linear arrays of dark puncta were observed on the cell surface and between cells (**Fig. 1H & I**) and

162   likely represent released virus particles (extracellular virions). Virus particles accumulate most of their

163   tegument in the cytoplasm and become enveloped before they are released from the cell. We measured

164   the width of nuclear capsids and extracellular virions from 8 tomograms to determine if they could be

165   distinguished based on their size (**Fig. 1J**). Nuclear capsids had a width of 125.8 ± 1.70 nm SEM (n=80

166   from 4 tomograms; range 96–160 nm; SD 15.22 nm), which is consistent with high-resolution structural

167   analysis of purified capsids[29] (~125 nm) and of capsids inside infected-cell nuclei[35]. Extracellular virions

168   were larger with a width of 198.6 ± 3.48 nm SEM (n=80 from 4 tomograms; range 128–272 nm; SD

169   31.15 nm), consistent with previous reports (~175-200 nm[28,36]). These differences were found to be

170   significant with a Wilcox test for unequal variance (W=126, *p*-value<$2.2×10^{-16}$).

7

171 *Early protein ICP0 and late protein gC have different patterns of spatiotemporal expression in HFF-*

172 *hTERT and U2OS cells*

173 Recent microscopy and single-cell transcriptomics studies have revealed that, even in a monolayer of

174 cultured cells synchronously infected with HSV-1, individual cells progress through the infection cycle

175 at different rates and the remodelling of cellular compartments varies depending on the stage of

176 infection[16,37]. To control for this, a recombinant strain of HSV-1 termed the timestamp virus has been

177 developed to allow identification of the stage of infection based on the abundance and subcellular

178 localization of the fluorescently tagged early and late viral proteins, ICP0 and gC respectively[16].

179 Fluorescence microscopy of HFF-hTERT cells infected with this timestamp virus allowed

180 characterization of the changes to cellular compartments that accompany progressing HSV-1 infection

181 and categorization of cells into 4 stages of infection. Having confirmed that virus particles could be

182 observed in infected HFF-hTERT cells using a 40 nm zone plate objective, we sought to obtain higher-

183 resolution information on the morphological changes exhibited by timestamp HSV-1-infected cells over

184 the course of infection by cryoSXT imaging using a 25 nm zone plate objective. However, preliminary

185 experiments performed using infected HFF-hTERT cells were unsuccessful as the infected cells proved

186 sensitive to higher flux density of the resultant X-ray beam, leading to localized sample heating and

187 low-quality tomograms. We therefore turned to U2OS osteosarcoma cells, which have been shown to

188 produce consistently high-quality tomograms when imaged by cryoSXT[25,26] and have been used

189 previously for HSV-1 ultrastructural analysis[38,39].

190 To compare the temporal profiles of progression of timestamp HSV-1 infection in HFF-hTERT and

191 U2OS cells, we first compared the expression patterns of these proteins between the two cell types.

192 Cells were infected at a multiplicity of infection (MOI) of 1 and 3 and samples were fixed at multiple time

193 points following infection before imaging on a widefield fluorescence microscope (**Fig. 2**). The

194 immediate early HSV-1 protein ICP0 was used to characterize early stages of infection because it is

195 one of the first viral proteins to be expressed[40]. In both cell lines, eYFP-ICP0 was expressed in all four

196 stages and its localization was restricted to the nucleus in stage 1. However, the spatial localization of

197 eYFP-ICP0 differed between HFF-hTERT and U2OS cells in stages 2-4: in these stages of HFF-hTERT

198 cell infection, eYFP-ICP0 signal was observed to diminish in the nucleus and continue to increase in

199 the cytoplasm across these three stages, whereas greater retention of eYFP-ICP0 in the nucleus was

200   observed in U2OS cells throughout the entire course of infection (**Fig. 2A**). This may reflect differences

201   in cellular interactions for ICP0 in U2OS cells, which is consistent with previous observations

202   demonstrating that replication deficits demonstrated by ICP0-null strains of HSV-1 in human fibroblasts

203   are effectively complemented in U2OS cells[41]. Unlike eYFP-ICP0, the spatial expression of gC-mCherry

204   was similar between HFF-hTERT and U2OS cells. gC is a viral glycoprotein expressed at late stages

205   of virus replication[42] that is incorporated into nascent virus particles at sites of virus envelopment[43]. In

206   both cell types gC-mCherry was enriched at a juxtanuclear site in stage 3 but became dispersed

207   throughout the cytoplasm and at the plasma membrane by stage 4 (**Fig. 2A**).

208   Next, we probed whether progression through the replication cycle follows the same timecourse in HFF-

209   hTERT and U2OS cells by infecting with different MOIs and imaging at different times post-infection to

210   compare the proportion of infected cells at each stage of infection. Although the spatial expression of

211   gC-mCherry was similar, fewer U2OS cells transitioned between stages 3 and 4 compared to HFF-

212   hTERT cells at MOI 1 and 3, even by the 24-hour timepoint (**Fig. 2B**). Stage 4 is defined by the dispersal

213   of gC-mCherry throughout the cytoplasm and, given the colocalization of gC with Golgi markers 58K

214   protein and beta-1,4-galactosyltransferase 1, this dispersal is thought to arise via fragmentation of the

215   Golgi complex[16]. The reduced number of U2OS cells in stage 4 may suggest a delay in, or resistance

216   to, Golgi complex fragmentation. The partial cytoplasmic translocation of eYFP-ICP0 and the reduced

217   gC-mCherry dispersal complicated the distinction between stages 1 and 2, and between stages 3 and

218   4, respectively. As a result, we combined the stages into two broader early (1+2) and late (3+4) stages

219   in our study.

220   *Vesicles proliferate and mitochondria become elongated and branched during HSV-1 infection.*

221   To characterize the changes in morphology of cellular compartments that accompany different stages

222   of virus infection, U2OS cells were grown on holey-carbon EM grids before being infected (or mock

223   infected) with timestamp HSV-1 and cryogenically preserved by plunge freezing in liquid nitrogen-

224   cooled liquid ethane (**Fig. 3A**). Vitrified samples were analyzed by cryo-wide-field microscopy to classify

225   the stage of infection and then imaged using cryoSXT to correlate the stage of virus infection in a

226   specific cell with observed morphological changes (**Fig. 3B**). As the proportion of U2OS cells in the

227   early stages of infection (stages 1+2) was consistently lower than the proportion in late stages of

228   infection (stages 3+4; **Fig. 2B**), grids were infected at MOI 1 and plunge frozen at 9 hpi to achieve a

229   more balanced proportion of cells in early and late stages of infection.

230   In total, 139 SXT tomograms were reconstructed; 76 from uninfected cells alongside 22 and 41 from

231   cells at early- or late-stages of infection, respectively, across three independent replicates (**Table 1**).

232   Manual inspection of the resultant tomograms revealed that the 25 nm zone plate allows detection of

233   higher resolution features than is possible with the 40 nm zone plate, such as the lumen of the

234   endoplasmic reticulum, cytoskeletal filaments, and small membrane structures (**Supp. Fig. 1A-E**). The

235   observed width of nuclear capsids is very similar in infected HFF-hTERT cells imaged using the 40 nm

236   zone plate (**Fig. 1J**) or U2OS cells imaged using the 25 nm zone plate (**Supp. Fig. 1F**). The tomograms

237   collected from U2OS cells using the 25 nm zone plate were thus deemed suitable for identifying

238   changes to cellular compartments that occur during HSV-1 infection.

239   We observed that the HSV-1 infection does not affect the morphology of cellular compartments such

240   as the nucleus and lipid droplets. Despite the continuous budding and fusion of capsids at the inner and

241   outer nuclear membranes, we did not observe any obvious changes to the integrity of the nuclear

242   envelope. We occasionally observed bulging of the nuclear envelope into the cytoplasm (**Supp. Fig.**

243   **1G**) but this could be seen in both uninfected and infected cells. The size and abundance of lipid

244   droplets did not appear to differ between uninfected, cells and those at early- or late-stages of infection.

245   However, striking changes were observed in the size and dispersal of vesicles, and in the length and

246   connectivity of the mitochondrial network, between uninfected and infected cells, with the changes

247   becoming more pronounced in cells at late stages of infection (**Fig. 4&5 and Supp. Video 1**).

248   HSV-1 capsids are thought to interact with several types of vesicles in the cytoplasm, including *trans*-

249   Golgi network vesicles and endosomes, both of which have been implicated in secondary

250   envelopment[13]. There was a striking difference in the concentration of vesicles at the juxtanuclear

251   compartment between uninfected and infected cells (**Fig. 4A and Supp. Video 2**). Infected cells had a

252   greater number of vesicles in juxtanuclear regions than uninfected cells. To determine if there was a

253   difference in the size of vesicles between uninfected cells and those at early- or late-stages of infection

254   we developed *Contour*, a program to segment and quantitate cellular features in 3D volumes

255   (manuscript in preparation). The widest point of each vesicle in three dimensions from 4 tomograms for

256   each condition was measured (**Fig. 4B**). The mean vesicle width was higher for uninfected cells (802.23

257   ± 348.47 nm SD, N=96) than for early-stage (688.66 ± 271.76 nm SD, N=184) and late-stage (631.85

258   ± 270.60 nm SD, N=184) infected cells. The mean vesicle widths for each tomogram were compared

259   using a one-way ANOVA and Tukey test and the vesicle widths of uninfected cells were found to be

260   significantly different from early-stage (p=0.04) and late-stage (p=0.01) infected cells. The vesicle width

261   did not differ significantly between early-stage and late-stage infected cells (p=0.62).

262   Mitochondria were the most phenotypically diverse organelles monitored in this study. In most cases,

263   they were thin and possessed a dark matrix (**Fig. 5A**). However, occasionally there were cells that

264   contained swollen mitochondria with a lighter matrix with highly contrasting cristae (**Supp. Fig. 2A**),

265   similar to observations of mitochondria made by EM[44–46]. This swollen morphology is associated with

266   release of cytochrome *c* from porous mitochondria during apoptosis[44]. Mitochondria are known to

267   interact with lipid droplets, for example to acquire fatty acids for respiration[47]. Interestingly, we observed

268   that lipid droplets were less frequently in close apposition to swollen mitochondria than to mitochondria

269   possessing dark matrices (**Supp. Fig. 2B**). Swollen mitochondria were observed in each of the three

270   independent sets of cell growth, infection and plunge freezing experiments performed, but these swollen

271   mitochondria were most prevalent in the uninfected cells of replicate 3 (**Supp. Fig. 2C**). In uninfected

272   cells, non-swollen mitochondria were heterogeneous in shape, with numerous being small and

273   spherical or long and curved in the same cell. We observed branching in some elongated mitochondria.

274   However, mitochondria appeared less heterogenous in shape in infected cells, and were consistently

275   more elongated and branched (**Fig. 5B and C, Supp. Fig. 2D,** and **Supp. Video 3**), in line with previous

276   observations made using super-resolution fluorescence microscopy of HFF-hTERT cells infected with

277   the timestamp virus[16]. Segmentation of mitochondria using *Contour* demonstrated that the number of

278   points where mitochondria branch into two or more arms (branching nodes) was significantly increased

279   in cells at late stages of infection (20.5 ± 5.45 nodes SD; n = 15) compared to uninfected cells (7.0 ±

280   4.02 nodes SD; n = 15) (**Fig. 5C**). In some cases, the mitochondria fused into a single, branched

281   network (**Fig. 5A** and **Supp. Video 3**), providing a dramatic demonstration of the increase in

282   mitochondrial branching and decrease in number of distinct mitochondrial networks that accompanies

283   HSV-1 infection. It was also observed that the number of distinct mitochondria decreased in infected

284   cells, although ambiguity regarding the connectivity of mitochondrial networks that extend beyond the

285   tomogram field-of-view prevented precise quantitation of this effect.

Discussion

In this study, we used cryoSXT to monitor the production of nascent HSV-1 particles and observe changes in the architecture of cellular compartments during infection. The penetrating power of X-rays facilitates cryoSXT imaging throughout the depth of the cell, allowing rare or transient events to be captured such as the transit of nascent capsids through the nuclear envelope. Furthermore, the lack of requirement for contrast-enhancing agents or chemical fixation allows direct imaging of cellular compartments in a near-native state. We exploited these properties of cryoSXT to compare the morphology of cellular compartments between uninfected and infected U2OS cells, using a recombinant strain of HSV-1 expressing fluorescently tagged early and late viral proteins to identify the infection stage of individual cells within the infected population.

HFF-hTERT and U2OS cells are commonly used for the study of HSV-1 infection[16,38,39]. We had intended to use HFF-hTERT cells for this study, to allow comparison with super-resolution fluorescence microscopy studies[16], but found infected HFF-hTERT cells to be less amenable to interrogation by cryoSXT. We therefore explored the differences in the dynamics of viral infection between HFF-hTERT and U2OS cells using the timestamp virus. In general, the modifications to cellular compartments observed in this study largely replicated those observed in HFF-hTERT cells[16], suggesting the interactions between viral components and cellular compartments are broadly similar in these two cell types. We observed subtle differences between the infections in these cells, including a U2OS-specific reduction in the dispersion of gC-containing membranes and a change in the nuclear-to-cytoplasmic translocation of the early viral protein ICP0 (**Fig. 2**). Residues important for the nuclear import/export dynamics of ICP0 have previously been identified: ICP0 possesses a canonical nuclear localization signal at residues 500–506 and deletion of 57 residues from the C terminus abolishes nuclear export of ICP0[48]. Although residues important for trafficking of ICP0 have been mapped, the cellular proteins involved in ICP0 trafficking have yet to be identified. In this study, a higher intensity of eYFP-ICP0 was detected in the nucleus compared with the cytoplasm of infected U2OS cells at every timepoint. In contrast, higher cytoplasmic intensity of ICP0 is observed at late stages of infection in HFF-hTERT cells and other cell lines[16,49,50]. This suggests that the expression of host proteins that regulate nuclear import and/or export of ICP0 may differ in U2OS cells. Several host proteins have been identified to participate in the nuclear trafficking of EP0, the pseudorabies virus orthologue of ICP0: Ran, Importin $\alpha1$, $\alpha3$, $\alpha7$,

12

315   β1, and transportin-1[51]. Future work is required to identify whether U2OS cells are depleted or enriched

316   in proteins involved in nuclear import/export of ICP0, which may illuminate the mechanisms regulating

317   subcellular localisation of this important viral E3 ligase during infection.

318   Compared with uninfected U2OS cells, infected cells had a greater local concentration of detectable

319   vesicles in the juxtanuclear space (Figure 4), consistent with previous research into the distribution of

320   vesicles during HSV-1 infection. For instance, early endosomes and lysosomes have been shown to

321   accumulate at the juxtanuclear region during infection[16]. This reorganization of vesicle distribution may

322   be related to a change in microtubule dynamics during infection. Previous studies have shown that γ-

323   tubulin and pericentrin, which are components of the microtubule-organizing centre (MTOC), become

324   dispersed during infection, suggesting breakdown of the MTOC[52]. Thereafter microtubules polymerize

325   at multiple foci in the cytoplasm rather than at a single site and the growth rate, length, and stability of

326   nascent microtubules become reduced compared with uninfected cells[52]. As the morphology of

327   microtubules changes, the transport of vesicles towards the cell periphery may be obstructed, resulting

328   in the accumulation of vesicles in juxtanuclear regions that may partly explain the increased local

329   concentration of vesicles. An additional source of new vesicles may arise from the fragmentation of the

330   Golgi complex during HSV-1 infection[53]. Most of the evidence for Golgi fragmentation is based on the

331   dispersion of several Golgi markers (β-COP, Giantin, GM130, 58K protein, and beta-1,4-

332   galactosyltransferase 1) throughout the cytoplasm during HSV-1 infection as assessed by fluorescence

333   microscopy[16,17,53]. Golgi fragmentation has been studied to a lesser extent by ultrathin section EM,

334   revealing cisternae become swollen and separated during infection[17]. Golgi fragmentation is thought to

335   be a consequence of disrupted microtubule dynamics and can be induced by treatment with

336   nocodazole, an inhibitor of β-tubulin polymerization[53]. Although our results are consistent with these

337   observations, the lack of markers for different types of vesicles meant that we could not determine if

338   the vesicles we observed with SXT were Golgi-derived, of endosomal origin, or were unrelated to these

339   cellular compartments. We observed a reduction in the mean size of vesicles as the infection

340   progressed (Figure 4B), which could arise either from fragmentation of the Golgi complex into small

341   vesicles or an inability of small vesicles to be trafficked from the juxtanuclear region to their target

342   organelles via microtubule transport. Future work could focus on the use of fluorescent markers and

13

343 correlative cryoSIM and cryoSXT imaging to identify which cellular compartments are found with an

344 increased concentration at the juxtanuclear region[25,54].

345 The spatial resolution afforded by cryoSXT allowed us to easily distinguish individual mitochondria in

346 uninfected and infected U2OS cells. Consistent with previous studies of infected HFF-hTERT cells[16],

347 we observed that mitochondria became more elongated and branched as infection progresses and form

348 extensive networks in some cases (Figure 5). Branching of mitochondria can either occur via *de novo*

349 synthesis or by fusion of mitochondria[55,56]. Our observation that some cells at late stages of infection

350 contain just one single large network of mitochondria, rather than numerous highly branched but

351 disconnected mitochondrial networks, is consistent with fusion predominating over fission as a driver of

352 mitochondrial network formation.

353 There are several possible explanations for the change in mitochondrial morphology observed during

354 HSV-1 infection. Mitochondrial movement tends to occur along microtubules and this movement

355 influences mitochondrial fusion/fission dynamics. Fission can arise from divergent movement of

356 mitochondrial extensions along microtubules and fusion is supported by convergent movement of

357 mitochondria[57]. Nocodazole treatment to depolymerize microtubules blocks transport, fusion and fission

358 of mitochondria, and there is evidence that thin microtubule extensions develop when fission is

359 obstructed[58]. It is possible that fission of existing mitochondrial networks may be obstructed when

360 microtubules depolymerize during HSV-1 infection, and this may prevent the generation of small

361 mitochondria. Such changes to the microtubule network begin at 6 hpi and would thus be expected to

362 have a greater influence on mitochondrial morphology in the late stages of infection[52], consistent with

363 our observations. Alternatively, the morphological changes to mitochondria may reflect a cellular

364 response to increased respiratory demand[59]. An increase in ATP production can be achieved by

365 mitochondrial elongation, for example under conditions of stress such as hypoxia and starvation of

366 glucose metabolism[60,61]. An increase in respiration, including oxidative phosphorylation, has been

367 observed for the related herpesvirus human cytomegalovirus[62]. The increased number of elongated

368 mitochondria in cells at late stages of infection could facilitate an increase in ATP production during

369 infection. Increased oxidative stress provides a third plausible explanation for the observed changes in

370 mitochondrial morphology. Increased production of reactive oxygen species (ROS) during respiration

371 appears to be a common feature of viral infection that has been observed for hepatitis C virus,

14

372   respiratory syncytial virus and the herpesvirus Epstein-Barr virus[63–65]. One mechanism by which the

373   cell responds to oxidative stress is by fusion of undamaged and ROS-damaged mitochondria to allow

374   for compensatory effects by sharing resources needed for ATP production[56]. It is possible that the

375   increased fusion events we observed may have arisen in response to increased oxidative stress during

376   infection.

377   Although a change in energy metabolism may reflect a generalized response by the cell to infection,

378   several HSV-1 proteins have been reported to localize at mitochondria (pUL7, pUL16, pUS3,

379   pUL12.5), suggesting that HSV-1 directly modulates mitochondrial activity[66–69]. pUS3 inhibits the

380   activity of electron transport chain complexes II and III as early as 6 hpi[67] and pUL12.5 functions in

381   the depletion of mitochondrial DNA and downregulation of mitochondrial proteins, including ND6 and

382   COX2, as early as 4–8 hpi[68]. The functional consequences of pUL16 binding mitochondria are not

383   well characterized, although we note that a pUL16 mutant co-localized with mitochondrial fission

384   sites[69]. The precise mechanisms by which HSV-1 alters the architecture of mitochondria and the role

385   of specific viral proteins, versus virus-induced metabolic strain, thus remains unclear. Combining

386   metabolic profiling of infected cells with ultrastructural analysis of mitochondrial morphology, using

387   wild-type and mutant (knock-out) viruses, will help illuminate the factors that drive the dramatic

388   remodelling of mitochondria observed during HSV-1 infection and the functional consequences

389   thereof.

390   In conclusion, cryoSXT allows the detection HSV-1 capsids and virions in different subcellular locations,

391   such as the nucleus, perinuclear space, cytoplasmic vesicles, and cell surface. Use of the timestamp

392   HSV-1 reporter virus facilitated identification of individual cells at early or late stages of infection, and

393   we observed accumulation of vesicles at juxtanuclear assembly compartments plus the elongation and

394   branching of mitochondria in infected cells as infection progresses. The ability of cryoSXT to image the

395   entire depth of infected cells in a near-native state, with minimal sample processing, highlights its utility

396   as a tool for 3D imaging to identify changes in cellular architecture that accompany virus infection.

397

398

399   **Materials & Methods**

400   *Reagents*

401   250 nm gold colloid fiducials were purchased from BBI Solutions (EM.GC250, batch 026935). The

402   working mixture was prepared via sedimentation of 1 mL of stock solution by centrifugation (12×g, 5

403   mins, RT) and then resuspending the pellet in 50 µL HBSS. The fiducials were sonicated at 80 kHz

404   (100% power) and 6°C to prevent aggregation. 3 mm gold EM grids with a holey carbon film (R 2/2,

405   200 mesh) were purchased from Quantifoil (Cat# AU G200F1 finder, batches Q45352 & Q45353). Poly-

406   L-lysine was purchased from Sigma Aldrich (Cat# P4832).

407   *Cell Lines*

408   U2OS cells (ATCC HTB-96; RRID CVCL_0042) and human foreskin fibroblast cells immortalized with

409   human telomerase reverse transcriptase (HFF-hTERT cells)[70] were cultured in Dulbecco's Modified

410   Eagle's Medium (DMEM; Thermo Fisher Scientific, Cat# 450 11590366) supplemented with 10% (v/v)

411   fetal bovine serum (FBS; Capricorn, Cat#: FBS-11A), L-glutamine (Thermo Fisher Scientific, Cat#

412   25030081), and penicillin/streptomycin (10000 U/ml; Thermo Fisher Scientific, Cat# 15070063). Hanks'

413   Balanced Salt Solution (HBSS; Thermo Fisher Scientific, Cat# 14175095) and 0.25% Trypsin-EDTA

414   (Thermo Fisher Scientific, Cat# 25200056) were used to wash and detach adherent cells, respectively.

415   Cells were maintained in a humidified 5% CO_2 atmosphere at 37°C.

416   *Recombinant Viruses*

417   Infections were performed using recombinant HSV-1 strain KOS expressing either the endogenously

418   tagged viral proteins eYFP-VP26 and gM-mCherry (Figure 1) or the endogenously tagged viral proteins

419   eYFP-ICP0 and gC-mCherry (timestamp HSV-1, Figures 2-5 and Supplementary Figures 1-2)[16], to

420   allow distinction between early and late stages of infection in U2OS and HFF-hTERT cells, with the

421   exception of the leftmost panel in **Fig. 1l** for which a non-fluorescent wild-type HSV-1 strain KOS was

422   used. Virus stocks were prepared by infection of Vero cells at low MOI (0.01) for 3–5 days, until

423   cytopathic effect was evident, before scraping cells into the medium. The cells were frozen at -70°C,

424   thawed and sonicated at 50 amps for 40 seconds. Crude virus stocks were clarified by centrifugation at

425   3,200×g in a benchtop centrifuge, aliquoted, and viral titers of the aliquots were quantified on Vero and

426   U2OS cells as described previously (71).

427   *Infection Assays*

428   For widefield imaging at ambient temperatures, HFF-hTERT and U2OS cells were seeded directly in 6-

429   well plates overnight at 2×10^5 cells per well. The cells were infected with the recombinant HSV-1 at 1–

430   3 PFU per cell in a low volume of media (500 µL) and this was designated as the start time of infection.

431   To maximize adsorption of virus, cells were incubated in the low-volume media for 1 hour in a humidified

432   5% CO_2 atmosphere at 37°C and the plates were swirled every 15 minutes. The inoculum was diluted

433   to 2 mL with medium and cells were incubated for 9-, 12-, 16- or 24-hours in total. The cells were

434   washed twice with HBSS and were fixed with 4% (v/v) formaldehyde for 20 minutes. The fixed cells

435   were washed three times with HBSS before imaging.

436   For widefield imaging under cryogenic conditions and cryoSXT, EM grids were glow discharged and

437   treated with filtered poly-L-lysine for 10 minutes as described previously (26). 3×10^5 cells per well were

438   seeded in 6-well plates containing the treated EM grids and were incubated overnight. Subsequently,

439   the cells were infected with 1 PFU per cell of timestamp HSV-1 as described above and were incubated

440   for 9 hours alongside uninfected controls. The EM grids were overlaid with 2 µL of the gold fiducial

441   working mixture described in the Reagents section. A Leica EM GP2 plunge freezer was used to blot

442   the grids for 0.5–1 s at 30°C and 80% humidity. The grids were plunged into liquid nitrogen-cooled liquid

443   ethane and then transferred into liquid nitrogen storage before imaging.

444   *Widefield Microscopy*

445   For room temperature samples, a Zeiss AxioImager2 microscope with an achromatic 50× air objective

446   (Zeiss LD EC Epiplan-Neofluar 50x/0.55 DIC M27; NA=0.55; free working distance=9.1 mm) was used

447   to image fixed infected cells grown on plastic 6-well plates. Fluorescent images were collected using

448   the Zeiss 46 HE YFP filter (Excitation 500±25 nm, Emission 535±30 nm) and the Zeiss 64 HE mPlum

449   filter (Excitation 587±25 nm, Emission 647±70 nm).

450   For cryo-widefield microscopy, cells at early- and late-stages of infection were identified based on the

451   spatiotemporal expression of eYFP-ICP0 and gC-mCherry using a Zeiss AxioImager2 microscope with

452   an achromatic 50× objective (described above) without immersion. The microscope was equipped with

453   a liquid nitrogen cryostage (Linkam) to maintain the sample at 77 K during imaging. Each grid was

17

454 mapped in its entirety in the brightfield and fluorescent channels (Zeiss 46 HE YFP filter and HE mPlum

455 filter as described above) using the LINK software (Linkam Scientific).

456 *Cryo-Soft-X-Ray Tomography*

457 X-ray images were collected using an UltraXRM-S/L220c X-ray microscope (Carl Zeiss X-ray

458 Microscopy) at beamline B24 at the UK synchrotron Diamond Light Source. Grids were imaged in a

459 liquid nitrogen-cooled vacuum chamber and samples were illuminated with 500 eV X-rays ($\lambda = 2.48$ nm)

460 for 0.5 or 1 s per projection. The transmitted light was focused by diffraction using zone plate objectives

461 with nominal resolution limits of either 25 nm or 40 nm. The 25 nm zone plate offers higher resolution

462 but captures a smaller field of view (~10×10 μm) than the 40 nm zone plate (~16×16 μm). Transmitted

463 images were collected using a 1024B Pixis CCD camera (Princeton instruments). X-ray mosaic images

464 (7×7 images capturing 66.2×66.2 μm for the 25 nm objective and 106.0×106.0 μm for the 40 nm

465 objective) were collected from different areas on the grid to assess overall cell morphology. For

466 identification of early and late stages of infection, X-ray mosaics were compared with fluorescent

467 imaged acquired on the cryo-widefield microscope to identify specific infected cells. These mosaics

468 were also used to identify regions of interest for tomography. Tilt series of projections were collected

469 from these regions by rotating the sample around an axis normal to the incident X-ray beam by up to

470 120° in increments of 0.2° or 0.5° per image, with maximum tilt angles of −60° and +60° and −70° and

471 +70° for the 25nm and 40nm objective respectively. SXT tilt series were processed using IMOD (version

472 4.9.2)[31]. The images were aligned along a single axis. A coarse alignment was performed by cross-

473 correlation with a high frequency cut-off radius of 0.1. Coarsely aligned tilt series were further aligned

474 manually using gold fiducials and dark cellular compartments, such as lipid droplets. A boundary model

475 was generated to reorient the 3D data in case the sample was collected at an angle and final alignment

476 was performed using linear interpolation. Tomograms were generated using back projection followed

477 by 20 iterations of a simultaneous iterations reconstruction technique (SIRT)-like filter to reduce noise.

478 *Segmentation*

479 Mitochondria were segmented using *Contour*, a bespoke semi-automated segmentation and

480 quantitation tool developed with Python 3. Full details on *Contour* will be described elsewhere but,

481 briefly, *Contour* automatically segments high contrast features such as mitochondria by thresholding

482 and then applying a restriction on the minimum number of consecutive segmented pixels vertically and

18

483 horizontally. Next, gaps in the segmented volume can be filled in by running this algorithm in local

484 regions of interest. Separate elements in the segmented volume are differentiated by grouping of

485 neighbouring voxels together. The differentiated elements are colour coded and their volumes are

486 quantitated from the number of voxels. The edges of the segmented elements are smoothened in each

487 image plane by translating the image by one pixel in all eight cardinal and ordinal directions in the XY

488 plane and calculating the median pixel value for all these translations. A 3D Gaussian filter with a sigma

489 of 2 was also added using Fiji to further smoothen the elements[72]. In *Contour*, the width of each

490 segmented element was calculated by finding all the coordinates of voxels at the perimeter of

491 segmented elements and calculating the largest modulus between any two coordinates. Segmented

492 volumes of cytoplasmic vesicles were generated manually using the Segmentation Editor 3.0.3 ImageJ

493 plugin[72] and these were imported into *Contour* to differentiate between segmented elements and

494 quantitate the width of the vesicles. Segmented volumes were visualized in 3D using the 3D Viewer

495 plugin in ImageJ[72].

496 *Graphs and statistics*

497 Distributions of capsid and virion widths were illustrated using a Violin SuperPlot[73], with data grouped

498 by source tomograms. The stacked area plots for the proportion of infected cells at different stages of

499 infection were generated using the ggplot2 package[74] in R studio[75]. The distribution of vesicle widths

500 were illustrated using a SuperPlot[76], with data grouped by source tomograms. The numbers of

501 mitochondrial branch points (branching nodes) were illustrated using a Violin SuperPlot[73], with data

502 grouped by replicate. A two-tailed paired t-test was used to compare the width of the nuclear envelope

503 at a site of primary envelopment with the width of the nuclear envelope elsewhere on the same

504 tomogram using Excel (Microsoft). A Wilcox test for unequal variance was used to assess a significant

505 difference in the widths of capsids and virions using R Studio[75]. One-way ANOVA and Tukey tests were

506 used to assess significant differences in the mean vesicle width using Prism version 8.2.1 (GraphPad

507 Software) and in the number of mitochondrial branching nodes (using R Studio[75]).

508

19

Data Availability

520

521 Original imaging data for tomograms illustrated in the manuscript is deposited at the BioImage Archive

522 (https://www.ebi.ac.uk/biostudies/BioImages)   and   EMPIAR

523 (https://www.ebi.ac.uk/pdbe/emdb/empiar/). The accession numbers for the data are EMPIAR:

524 EMPIAR-XXXX, EMPIAR-XXXX, … and BioImage Archive: S-BIADXX, S-BIADXX, …. Additional tilt

525 series and tomograms used for quantitative analysis have been deposited with the University of

526 Cambridge Apollo Repository, available at https://doi.org/10.17863/CAM.XXXX.

527 **Table 1. Collection of cryoSXT data to analyse changes in cellular morphology accompanying**

528 **infection.** CryoSXT data was collected using a 25 nm zone plate from multiple uninfected cells or cells

529 at early and late stages of infection across three independent replicates. Tiled X-ray projections ('X-ray

530 mosaics') with a 66.2×66.2 µm field of view were collected at multiple areas on the sample grid to

531 identify cells of interest. Tilt series were collected at perinuclear or peripheral regions of the cytoplasm

532 within these cells and were processed to generate tomograms.

| Replicate	Stage of infection	X-ray mosaics	Cells in mosaics	Cells imaged by tomography	Tomograms
1	Uninfected	19	30	18	29
	Early	4	4	2	4
	Late	8	13	10	14
2	Uninfected	10	20	14	20
	Early	9	13	11	13
	Late	10	10	8	12
3	Uninfected	8	27	26	27
	Early	6	7	5	5
	Late	8	13	13	15

533

21

534
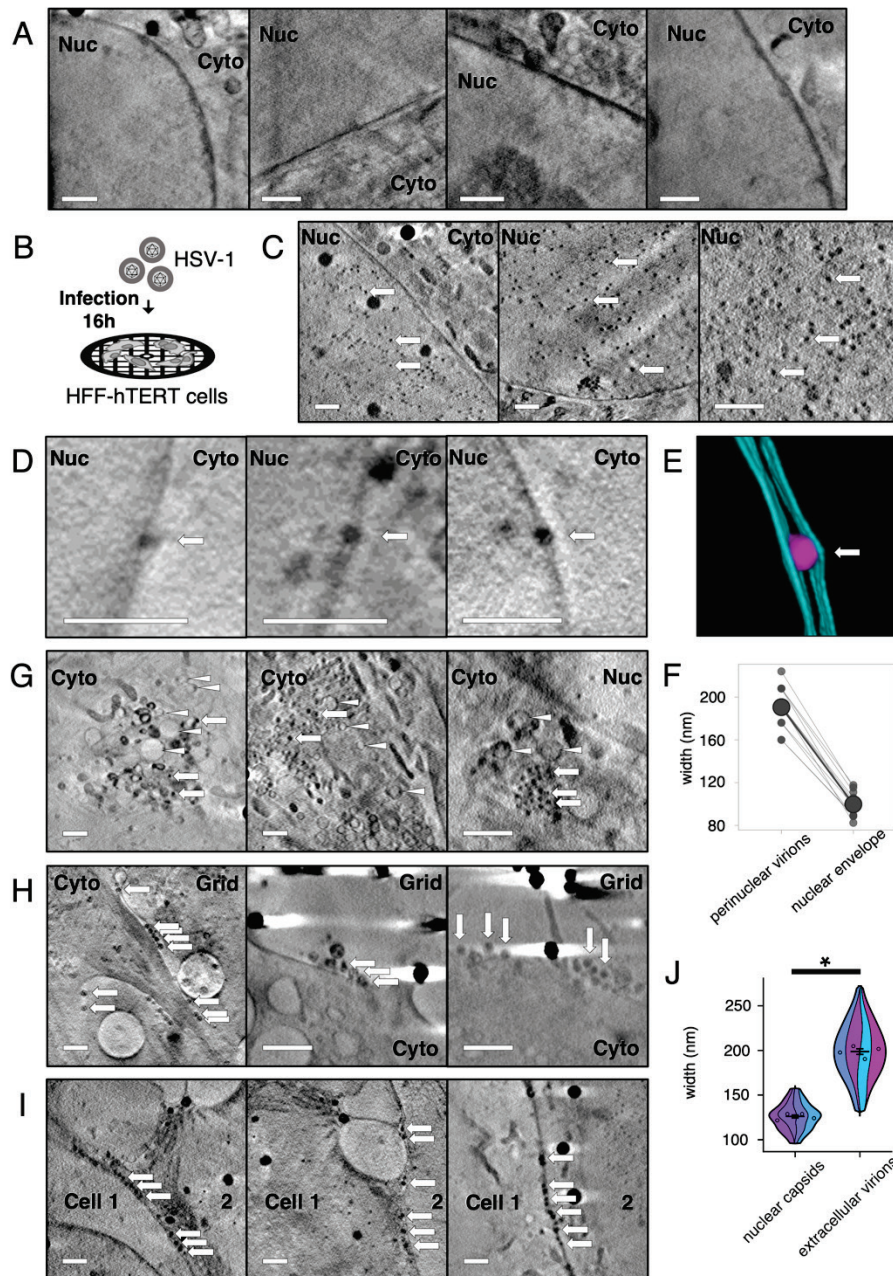
Fig. 1. Soft X-ray tomography imaging at cryogenic temperatures of HSV-1-infected HFF-hTERT cells identifies virus particles. HFF-hTERT cells were grown on EM grids and plunge frozen 16 hpi with 2 plaque-forming units of HSV-1 per cell or mock infection. All tomograms were reconstructed from X-ray projections collected using zone plate objective optics affording 25 nm (**A**) or 40 nm (**C, D, G–I**) resolution; scale bars = 1 μm. (**A**) The nucleus (Nuc) has a largely uniform X-ray absorbance in uninfected HFF-hTERT cells. Cyto, cytoplasm. (**B**) Schematic of infection workflow. (**C**) In HSV-1 infected cells many dark puncta are evident in the nucleus, consistent with these puncta being newly assembled HSV-1 capsids. (**D**) Dark puncta were also observed within the perinuclear space of the

22

543   nuclear envelope, consistent with these being HSV-1 capsids undergoing primary envelopment/de-

544   envelopment to leave the nuclear space. (**E**) Segmentation of a perinuclear viral particle (magenta) and

545   the two membranes of the nuclear envelope (cyan). The perinuclear viral particle distends the nuclear

546   envelope. (**F**) The width of perinuclear viral particles plus associated membranes is 190.5 ± 6.01 nm

547   SEM (N=11; 20.8 nm SD), which is greater than the width of the nuclear membrane elsewhere (99.8 ±

548   3.57 nm SEM; N=11; 11.9 nm SD). (**G**) HSV-1 capsids (arrows) were also observed in the cytoplasm

549   alongside vesicles (arrowheads). (**H**) Multiple particles are observed along the surface of infected cells,

550   consistent with these being assembled HSV-1 virions that have exited the infected cell. (**I**) HSV-1 virions

551   are also observed at the junctions between cells. (**J**) The width of the nuclear capsids is 125.8 ± 1.70

552   nm SEM (n=80 from 4 tomograms), consistent with these being HSV-1 capsids (~125 nm[28,29]). The

553   width of the extracellular virions is 198.6 ± 3.48 nm SEM (n=80 from 4 tomograms), consistent with

554   these being fully-enveloped HSV-1 virions (~200 nm[36]). Due to unequal variance, a Wilcox test was

555   performed to determine a significant difference in the width of nuclear capsids and extracellular virions

556   (W=126, *p*-value<2.2×10^{-16}). Error bars show mean ± SEM.

557
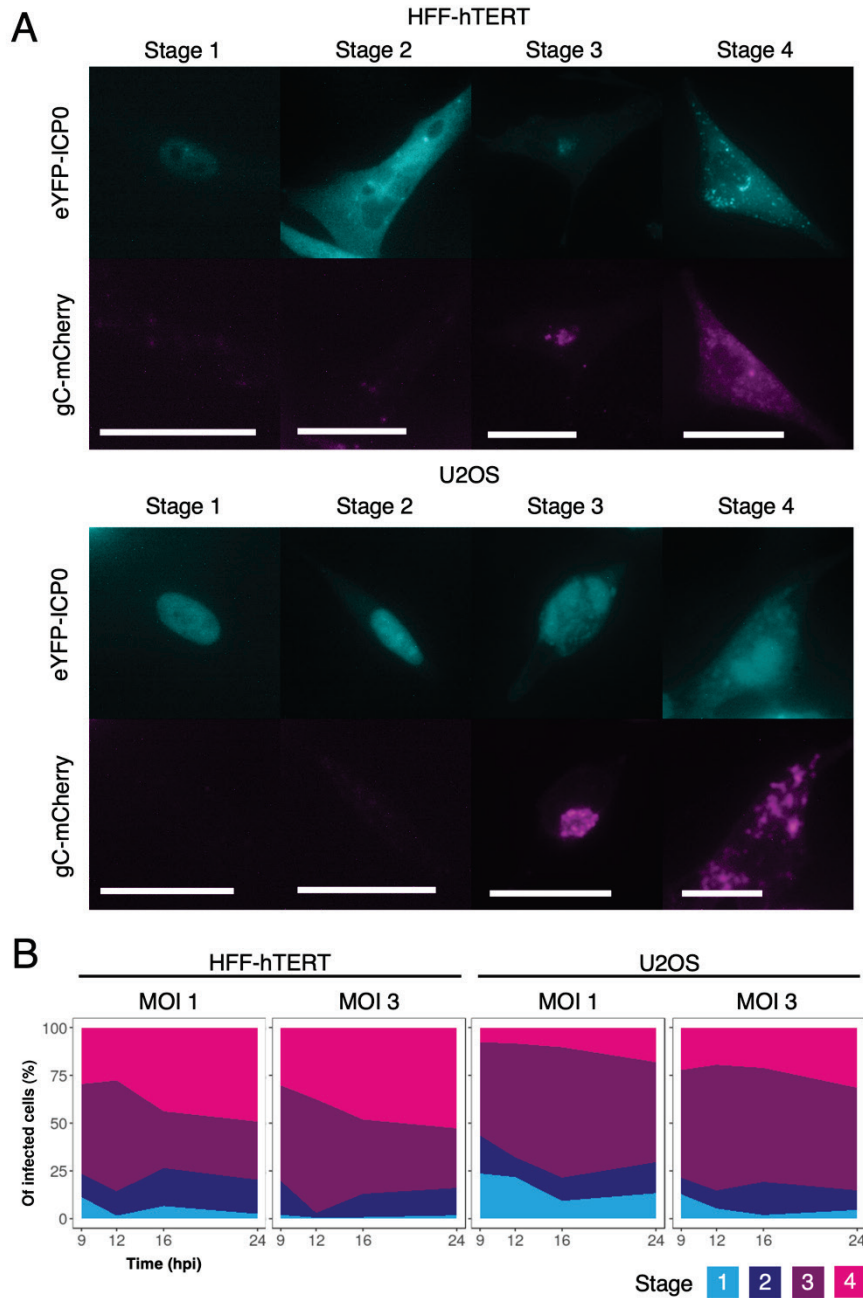
Fig. 2. Temporal analysis of HSV-1 infection using the dual-fluorescent timestamp virus. (**A**) Room temperature widefield fluorescence imaging of timestamp HSV-1 infected HFF-hTERT and U2OS cells was used to delineate between four stages of infection based on the expression and localization of the early protein eYFP-ICP0 and the late protein gC-mCherry[16]. The spatiotemporal expression of these fusion proteins was similar in HFF-hTERT and U2OS cells, except for partial retention of eYFP-ICP0 in the nucleus of U2OS cells during stages 2–4. Scale bars = 50 μm. (**B**) The proportion of infected cells in each stage was determined using widefield imaging and different multiplicities of infection (MOIs) in HFF-hTERT and U2OS cells at 9, 12, 16, and 24 hpi.

24

567

568
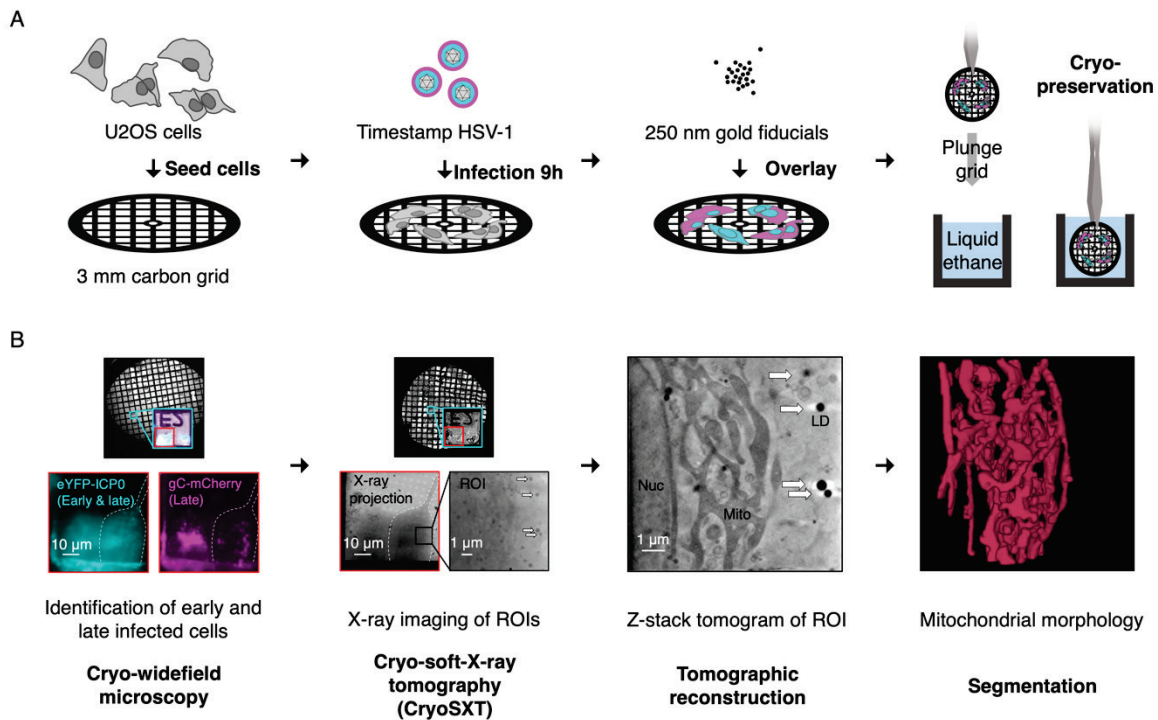
Fig. 3. Workflow for multi-modal imaging of HSV-1 infected cells. (**A**) Preparation of infected cells samples for multimodal imaging. U2OS cells are cultured on holey-carbon EM grids and infected with recombinant 'timestamp' HSV-1, expressing fluorescently tagged proteins eYFP-ICP0 and gC-mCherry that allow identification of the stage of infection for each cell under investigation. At 9 hpi, gold fiducials are overlayed onto the sample to facilitate image registration and grids are cryopreserved in a near-native state by plunge freezing in liquid ethane. (**B**) Multi-modal imaging of infected U2OS cells. A widefield microscope with a cryo stage is used to locate the grid positions of infected cells. The stage of infection for each cell is determined based on the differential expression and localisation of the eYFP-ICP0 and gC-mCherry (as shown in **Fig. 2**). These grids are then loaded into the cryo-soft-X-ray microscope at Diamond Light Source beamline B24 and are illuminated with soft X-rays at the marked grid positions. X-ray projections of regions of interest (ROIs) are collected at multiple angles and aligned using the gold fiducials and intracellular features, such as lipid droplets (LDs), with the program IMOD[31]. Tomograms are reconstructed from these projections using IMOD to compare intracellular morphology between uninfected cells and those at early- or late-stages of infection. Segmentation facilitates quantitation and visualization in three dimensions of the observed cellular structures.
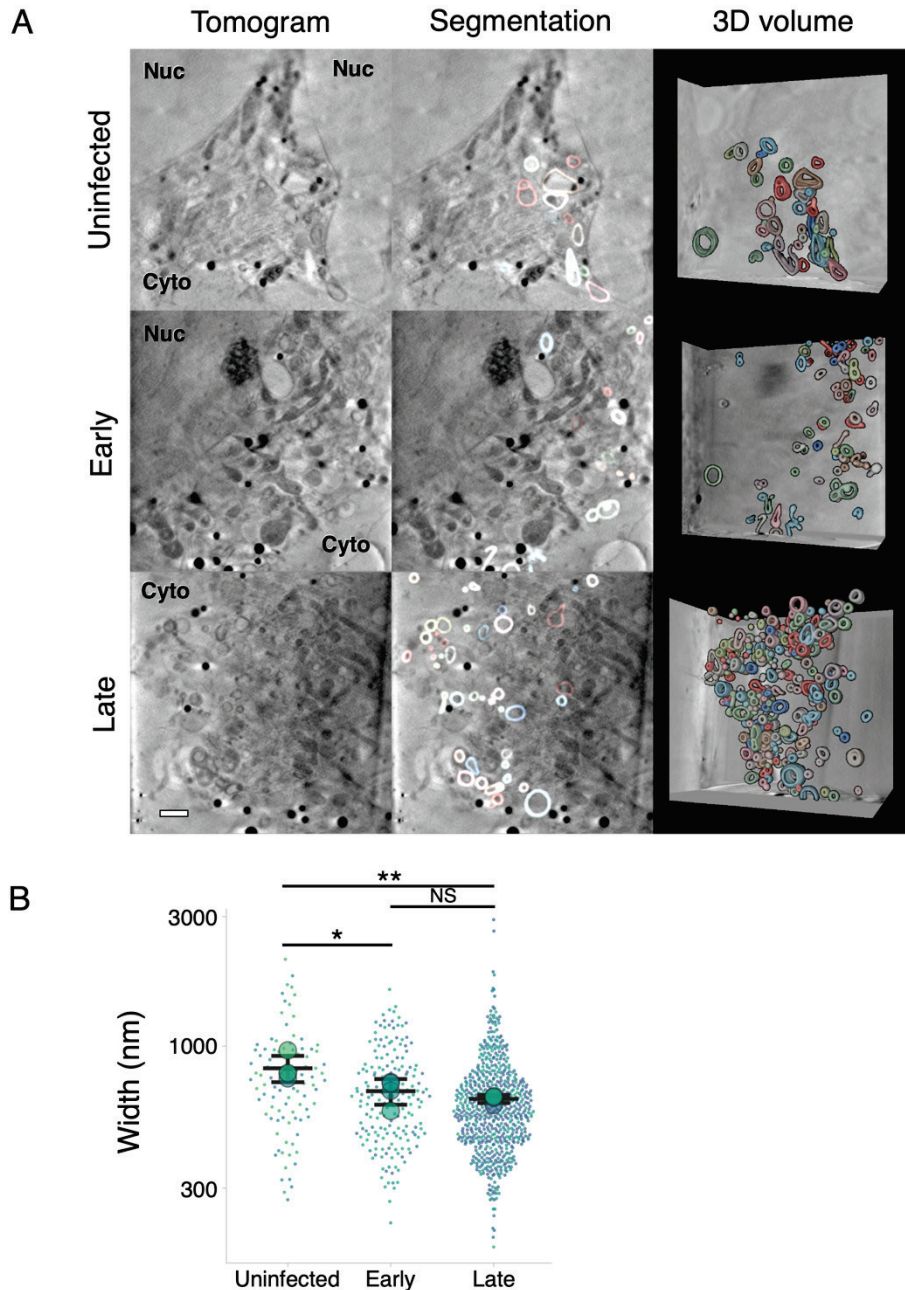
25

Fig. 4. Remodelling of cytoplasmic vesicles during HSV-1 infection. CryoSXT tomograms were recorded of cells classified as uninfected, early-stage infection (stages 1+2) or late-stage infection (stages 3+4) with timestamp HSV-1 based on fluorescent cryo-wide field microscopy. Data are representative of three independent experiments. Scale bar = 1 μm. (**A**) A higher concentration of vesicles is observed at the juxtanuclear compartment in cells at early- or late-stages of infection compared with uninfected cells. (**B**) The maximum width of each vesicle in three-dimensions was measured in *Contour* (manuscript in preparation). Vesicles with a spherical, ellipsoidal, or dumbbell shape were included in the analysis but vesicles with a shape that didn't fall into these categories were

26

593   excluded. Intra-luminal vesicles and vesicles that were not individually resolved by the segmentation

594   were also excluded from the analysis. Significance of differences was assessed with a one-way ANOVA

595   and Tukey tests for the combinations: uninfected-early (p=0.04), uninfected-late (p=0.01), and early-

596   late (p=0.62). Big circles show the mean vesicle width per tomogram (4 tomograms per condition). Error

597   bars show overall mean ± SD.

598

599
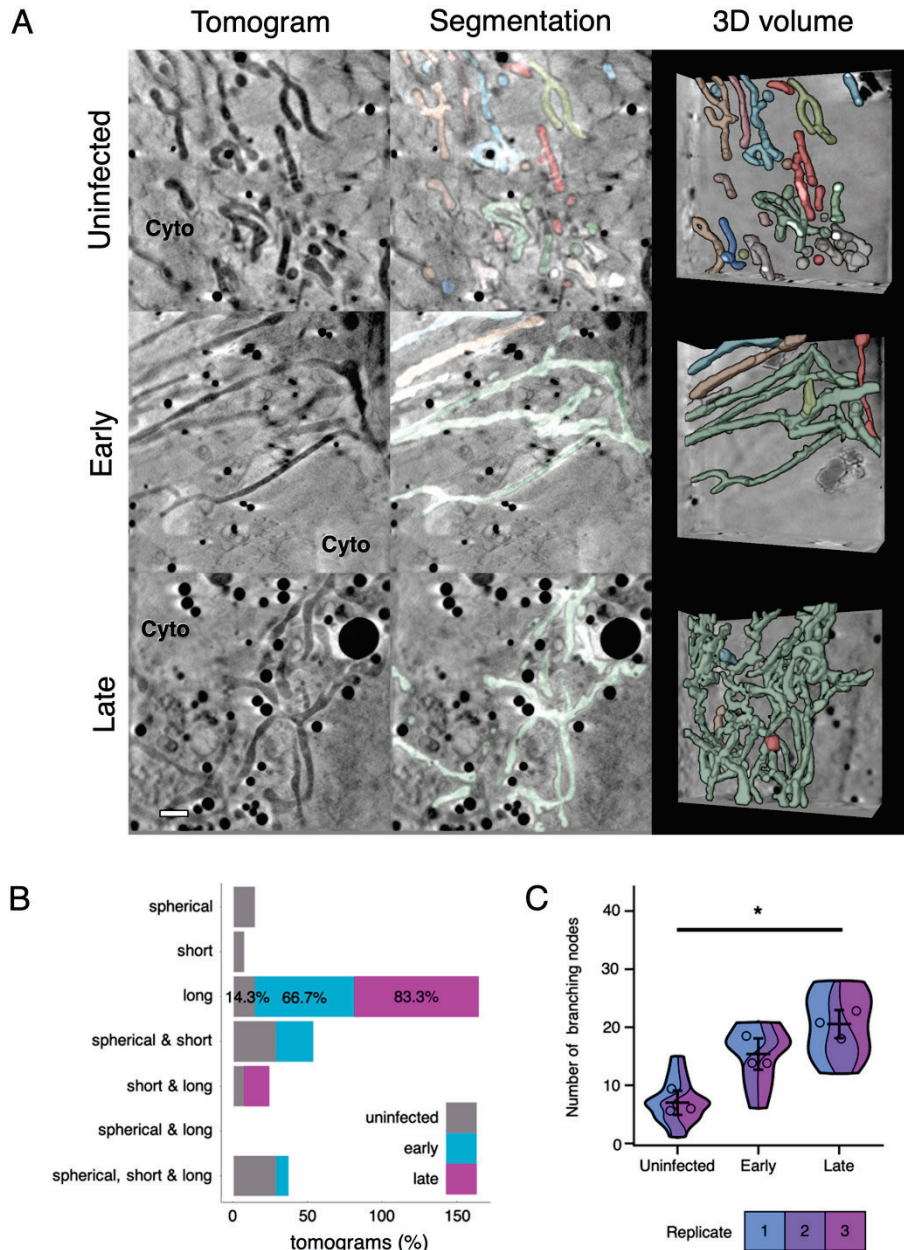
Fig. 5. Remodelling of mitochondria during HSV-1 infection. Morphological changes to mitochondria were assessed from cryoSXT tomograms collected from uninfected cells and cells at early- or late-stages of infection with timestamp HSV-1. Data are representative of three independent experiments. Scale bars = 1 μm. (**A**) A shift towards elongated and branched mitochondria was observed during infection. Mitochondria were segmented and differentiated using *Contour* to highlight the abundance and 3D geometry of individual mitochondria. (**B**) The percentages of tomograms with long mitochondria were greater for cells at early- or late-stages of infection than for uninfected cells in replicate 2. Mitochondrial morphology was more heterogenous in uninfected cells. See **Supp. Fig 2** for

28

608   equivalent data from replicates 1 and 3. (**C**) The numbers of branching nodes were calculated for 45

609   tomograms across all replicates and significant differences in the number of nodes between uninfected

610   cells and those at late stages of infection were determined for each replicate using ANOVA and Tukey

611   tests (p <0.05). Error bars show mean ± SD.

612

613
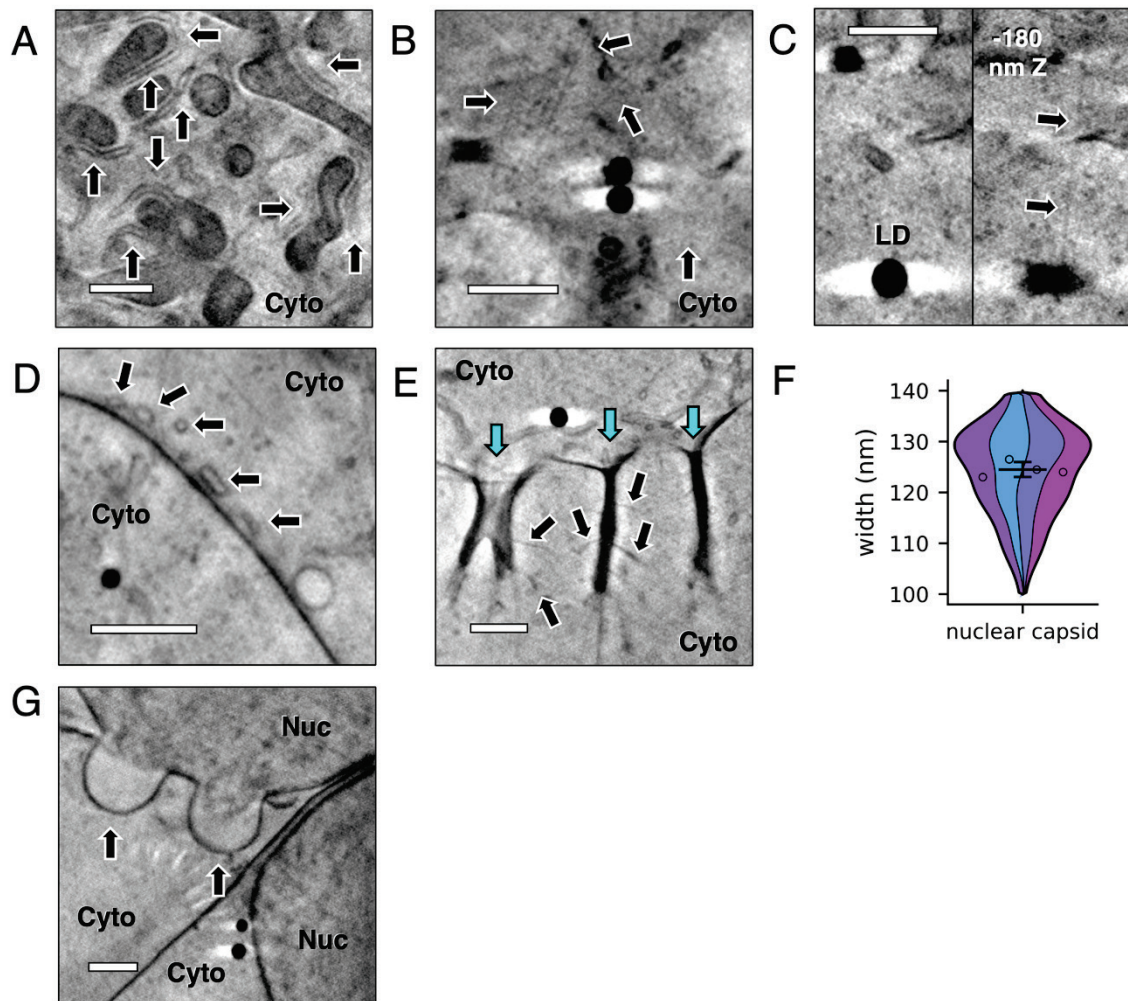
Supp. Fig. 1. High resolution structures visible with the 25 nm zone plate objective. 139 CryoSXT tomograms were recorded from 107 cells using a 25 nm zone plate (ZP) objective and several structures that were unrelated to HSV-1 infection were observed, including some that were not visible using the 40 nm zone plate objective. (**A**) The endoplasmic reticulum (ER) forms a silhouette (arrows) around the mitochondria and the ER lumen is visible with the 25 nm zone plate. Cyto, cytoplasm. (**B**) Linear structures resembling cytoskeletal filaments are visible with the 25 nm zone plate (arrows). (**C**) A putative cytoskeletal filament (arrows) is in close apposition to a lipid droplet (LD) and may represent a physical interaction. (**D**) Small vesicles with widths of 150–300 nm in the peripheral cytoplasm are observed (arrows). (**E**) Large internalisations of the plasma membrane with depths of 1.6–2.2 µm (cyan) and smaller side extensions (black arrows) are visible and may represent events of clathrin-independent bulk endocytosis[77]. (**F**) The width of nuclear capsids was remeasured after imaging with the 25 nm zone plate: 124.5 nm ± 0.96 nm SEM (n=80 from 4 tomograms; 8.55 nm SD). (**G**) Bulging of the nuclear envelope is observed (arrows). We initially observed these in HSV-1 infection and thought it may

30

627   represent a virus-directed decrease in the integrity of the nuclear envelope, but we found multiple

628   examples in uninfected cells suggesting that they are a general feature of U2OS cells. Nuc, nucleus.

629

630
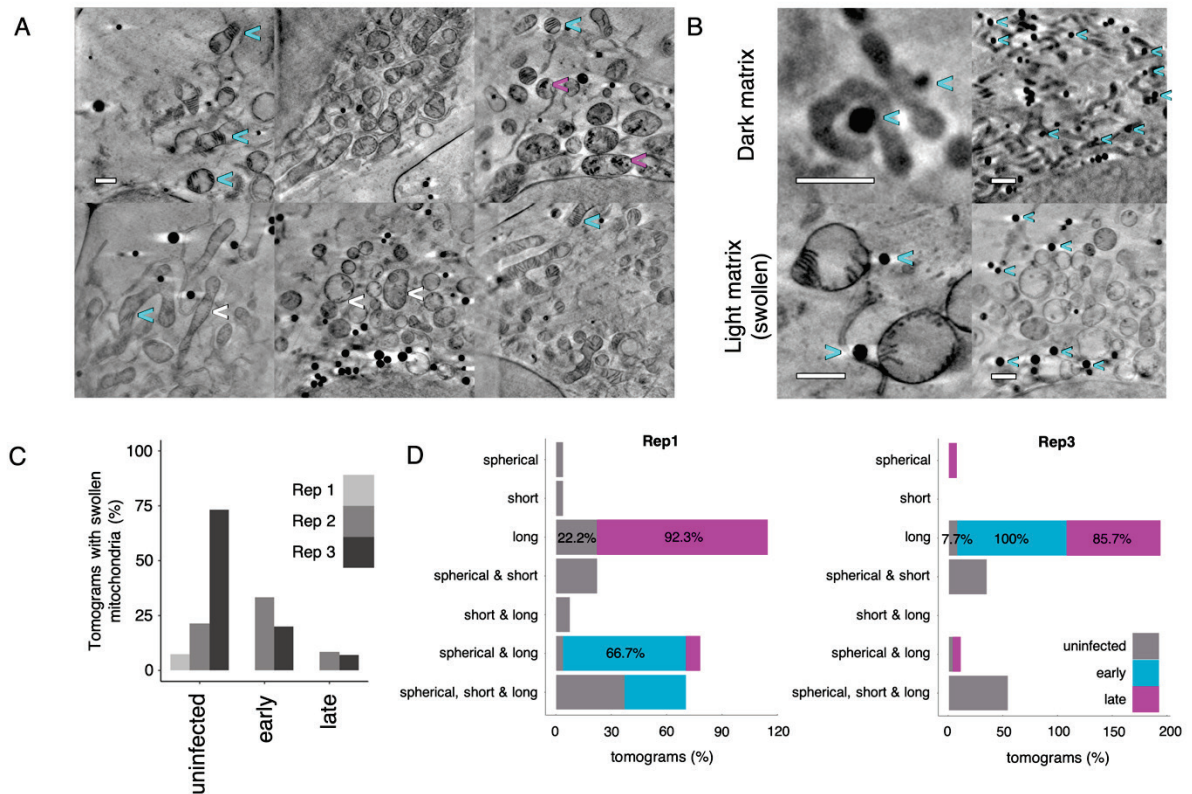
631

632 **Supp. Fig. 2. The heterogenous morphology of mitochondria.** Heterogenous mitochondrial

633 morphologies are observed in cryoSXT tomograms collected from uninfected cells and cells at early

634 and late stages of infection with timestamp HSV-1. Scale bars = 1 μm. (**A**) In some cases, mitochondria

635 have light matrices with highly contrasting cristae (cyan arrows). This "swollen" phenotype has been

636 reported to occur during cytochrome *c* release from porous mitochondria during apoptosis[44]. Dark

637 matter is also observed in the matrix (magenta arrows) and may represent vesiculation. Small dark

638 puncta are present in the matrix (white arrows) and could represent vesicles or short cristae. (**B**)

639 Mitochondria with dark matrices were commonly coupled with lipid droplets (cyan arrows) but most lipid

640 droplets were uncoupled from swollen mitochondria. (**C**) The percentages of tomograms with swollen

641 mitochondria for uninfected cells and cells at early- or late-stages of infection in three independent

642 replicates. (**D**) The percentages of tomograms collected from uninfected cells and those at early- or

643 late-stages on infection in replicates 1 and 3 that contain different combinations of mitochondrial

644 morphologies.

32

645 **Supp. Video 1. Segmentation of vesicles and mitochondria in the cytoplasm of a cell at a late**

646 **stage of infection.** CryoSXT data was collected from U2OS cells infected for 9 hours with 1 plaque-

647 forming unit per cell of the timestamp HSV-1 virus. Cryo-fluorescence microscopy revealed that this cell

648 was at a late stage of infection. The mitochondria were segmented using *Contour* and separate

649 mitochondria are colour-coded in shades of orange, red, pink and purple. Cytoplasmic vesicles were

650 segmented using *Segmentation Editor* in *ImageJ*. The vesicles were later differentiated and color-coded

651 using *Contour* and are displayed here in shades of blue and green. Field of view is 9.46×9.46 µm.

652 **Supp. Video 2. Segmentation of cytoplasmic vesicles reveals the effect of HSV-1 infection on**

653 **vesicle concentration at juxtanuclear sites.** CryoSXT data was collected from uninfected U2OS cells

654 and U2OS cells infected for 9 hours with 1 plaque-forming unit per cell of the timestamp HSV-1 virus.

655 Cytoplasmic vesicles were segmented using *Segmentation Editor* in *ImageJ*. The vesicles were later

656 differentiated and colour-coded using *Contour*. Fields of view are 9.46×9.46 µm.

657 **Supp. Video 3. Segmentation of mitochondria reveals the effect of HSV-1 infection on**

658 **mitochondrial morphology.** CryoSXT data was collected from uninfected U2OS cells and U2OS cells

659 infected for 9 hours with 1 plaque-forming unit per cell of the timestamp HSV-1 virus. Mitochondria were

660 segmented and colour-coded using *Contour* and appear elongated and branched in cells at late stages

661 of infection. Fields of view are 9.46×9.46 µm.

662

663 **References**

664 1. Nicoll, M. P., Proença, J. T. & Efstathiou, S. The molecular basis of herpes simplex virus latency.
665   *FEMS Microbiol. Rev.* **36**, 684–705 (2012).

666 2. Owen, D., Crump, C. & Graham, S. Tegument Assembly and Secondary Envelopment of
667   Alphaherpesviruses. *Viruses* **7**, 5084–5114 (2015).

668 3. Ahmad, I. & Wilson, D. W. HSV-1 Cytoplasmic Envelopment and Egress. *Int. J. Mol. Sci.* **21**, 5969
669   (2020).

670 4. Mettenleiter, T. C. Herpesvirus Assembly and Egress. *J. Virol.* **76**, 1537–1547 (2002).

671 5. Johnson, D. C. & Baines, J. D. Herpesviruses remodel host membranes for virus egress. *Nat. Rev.*
672   *Microbiol.* **9**, 382–394 (2011).

673 6. Crump, C. Virus Assembly and Egress of HSV. in *Human Herpesviruses* (eds. Kawaguchi, Y.,
674   Mori, Y. & Kimura, H.) 23–44 (Springer Singapore, 2018). doi:10.1007/978-981-10-7230-7_2.

675 7. Brown, J. C. & Newcomb, W. W. Herpesvirus capsid assembly: insights from structural analysis.
676   *Curr. Opin. Virol.* **1**, 142–149 (2011).

677 8. Bigalke, J. M. & Heldwein, E. E. Structural basis of membrane budding by the nuclear egress
678   complex of herpesviruses. *EMBO J.* **34**, 2921–2936 (2015).

679 9. Bigalke, J. M. & Heldwein, E. E. The Great (Nuclear) Escape: New Insights into the Role of the
680   Nuclear Egress Complex of Herpesviruses. *J. Virol.* **89**, 9150–9153 (2015).

681 10. Bigalke, J. M. & Heldwein, E. E. Nuclear Exodus: Herpesviruses Lead the Way. *Annu. Rev. Virol.*
682   **3**, 387–409 (2016).

683 11. Zeev-Ben-Mordehai, T. *et al.* Crystal Structure of the Herpesvirus Nuclear Egress Complex
684   Provides Insights into Inner Nuclear Membrane Remodeling. *Cell Rep.* **13**, 2645–2652 (2015).

685 12. Hernández Durán, A. *et al.* Protein interactions and consensus clustering analysis uncover insights
686   into herpesvirus virion structure and function relationships. *PLOS Biol.* **17**, e3000316 (2019).

687 13. Hollinshead, M. *et al.* Endocytic tubules regulated by Rab GTPases 5 and 11 are used for
688   envelopment of herpes simplex virus. *EMBO J.* **31**, 4204–4220 (2012).

689 14. Kotsakis, A., Pomeranz, L. E., Blouin, A. & Blaho, J. A. Microtubule Reorganization during Herpes
690   Simplex Virus Type 1 Infection Facilitates the Nuclear Localization of VP22, a Major Virion Tegument
691   Protein. *J. Virol.* **75**, 8697–8711 (2001).

692   15. Kim, J. A. *et al.* HSV-1 ICP27 induces apoptosis by promoting Bax translocation to mitochondria
693   through interacting with 14-3-3θ. *BMB Rep.* **50**, 257–262 (2017).

694   16. Scherer, K. M. *et al.* A fluorescent reporter system enables spatiotemporal analysis of host cell
695   modification during herpes simplex virus-1 replication. *J. Biol. Chem.* **296**, 100236 (2021).

696   17. Martin, C. *et al.* Herpes Simplex Virus Type 1 Neuronal Infection Perturbs Golgi Apparatus Integrity
697   through Activation of Src Tyrosine Kinase and Dyn-2 GTPase. *Front. Cell. Infect. Microbiol.* **7**, 371
698   (2017).

699   18. Maeda, F. *et al.* Herpes Simplex Virus 1 UL34 Protein Regulates the Global Architecture of the
700   Endoplasmic Reticulum in Infected Cells. *J. Virol.* **91**, (2017).

701   19. Ayache, J., Beaunier, L., Boumendil, J., Ehret, G. & Laub, D. Artifacts in Transmission Electron
702   Microscopy. in *Sample Preparation Handbook for Transmission Electron Microscopy* 125–170
703   (Springer New York, 2010). doi:10.1007/978-0-387-98182-6_6.

704   20. Schnell, U., Dijk, F., Sjollema, K. A. & Giepmans, B. N. G. Immunolabeling artifacts and the need
705   for live-cell imaging. *Nat. Methods* **9**, 152–158 (2012).

706   21. Büttner, M. *et al.* Challenges of Using Expansion Microscopy for Super-resolved Imaging of
707   Cellular Organelles. *ChemBioChem* **22**, 686–693 (2021).

708   22. Harkiolaki, M. *et al.* Cryo-soft X-ray tomography: using soft X-rays to explore the ultrastructure of
709   whole cells. *Emerg. Top. Life Sci.* **2**, 81–92 (2018).

710   23. Lewis, R. A. Medical phase contrast x-ray imaging: current status and future prospects. *Phys. Med.*
711   *Biol.* **49**, 3573–3583 (2004).

712   24. Garman, E. F. Developments in X-ray Crystallographic Structure Determination of Biological
713   Macromolecules. *Science* **343**, 1102–1108 (2014).

714   25. Kounatidis, I. *et al.* 3D Correlative Cryo-Structured Illumination Fluorescence and Soft X-ray
715   Microscopy Elucidates Reovirus Intracellular Release Pathway. *Cell* **182**, 515-530.e17 (2020).

716   26. Okolo, C. A. *et al.* Sample preparation strategies for efficient correlation of 3D SIM and soft X-ray
717   tomography data at cryogenic temperatures. *Nat. Protoc.* **16**, 2851–2885 (2021).

718   27. Pérez-Berná, A. J. *et al.* Structural Changes In Cells Imaged by Soft X-ray Cryo-Tomography
719   During Hepatitis C Virus Infection. *ACS Nano* **10**, 6597–6611 (2016).

720   28. Laine, R. F. *et al.* Structural analysis of herpes simplex virus by optical super-resolution imaging.
721   *Nat. Commun.* **6**, 5980 (2015).

722   29.   Yuan, S. *et al.* Cryo-EM structure of a herpesvirus capsid at 3.1 Å. *Science* **360**, eaao7283 (2018).

723   30.   von Hofsten, O. *et al.* Sub-25-nm laboratory x-ray microscopy using a compound Fresnel zone
724   plate. *Opt. Lett.* **34**, 2631 (2009).

725   31.   Mastronarde, D. N. & Held, S. R. Automated tilt series alignment and tomographic reconstruction
726   in IMOD. *J. Struct. Biol.* **197**, 102–113 (2017).

727   32.   Blondeau, C. *et al.* Tetherin Restricts Herpes Simplex Virus 1 and Is Antagonized by Glycoprotein
728   M. *J. Virol.* **87**, 13124–13133 (2013).

729   33.   Zenner, H. L., Mauricio, R., Banting, G. & Crump, C. M. Herpes simplex virus 1 counteracts tetherin
730   restriction via its virion host shutoff activity. *J. Virol.* **87**, 13115–13123 (2013).

731   34.   Johnson, D. C., Webb, M., Wisner, T. W. & Brunetti, C. Herpes Simplex Virus gE/gI Sorts Nascent
732   Virions to Epithelial Cell Junctions, Promoting Virus Spread. *J. Virol.* **75**, 821–833 (2001).

733   35.   Vijayakrishnan, S., McElwee, M., Loney, C., Rixon, F. & Bhella, D. In situ structure of virus capsids
734   within cell nuclei by correlative light and cryo-electron tomography. *Sci. Rep.* **10**, 17596 (2020).

735   36.   Grünewald, K. *et al.* Three-Dimensional Structure of Herpes Simplex Virus from Cryo-Electron
736   Tomography. *Science* **302**, 1396–1398 (2003).

737   37.   Drayman, N., Patel, P., Vistain, L. & Tay, S. HSV-1 single-cell analysis reveals the activation of
738   anti-viral and developmental programs in distinct sub-populations. *eLife* **8**, e46339 (2019).

739   38.   Simpson-Holley, M., Colgrove, R. C., Nalepa, G., Harper, J. W. & Knipe, D. M. Identification and
740   Functional Evaluation of Cellular and Viral Factors Involved in the Alteration of Nuclear Architecture
741   during Herpes Simplex Virus 1 Infection. *J. Virol.* **79**, 12840–12851 (2005).

742   39.   Deng, Z. *et al.* HSV-1 Remodels Host Telomeres to Facilitate Viral Replication. *Cell Rep.* **9**, 2263–
743   2278 (2014).

744   40.   Cai, W. & Schaffer, P. A. Herpes simplex virus type 1 ICP0 regulates expression of immediate-
745   early, early, and late genes in productively infected cells. *J. Virol.* **66**, 2904–2915 (1992).

746   41.   Deschamps, T. & Kalamvoki, M. Impaired STING Pathway in Human Osteosarcoma U2OS Cells
747   Contributes to the Growth of ICP0-Null Mutant Herpes Simplex Virus. *J. Virol.* **91**, (2017).

748   42.   Visalli, R. J. & Brandt, C. R. The HSV-1 UL45 18 kDa gene product is a true late protein and a
749   component of the virion. *Virus Res.* **29**, 167–178 (1993).

43. Loret, S., Guay, G. & Lippé, R. Comprehensive Characterization of Extracellular Herpes Simplex Virus Type 1 Virions. *J. Virol.* **82**, 8605–8618 (2008).

44. Sun, M. G. *et al.* Correlated three-dimensional light and electron microscopy reveals transformation of mitochondria during apoptosis. *Nat. Cell Biol.* **9**, 1057–1065 (2007).

45. Miyazono, Y. *et al.* Uncoupled mitochondria quickly shorten along their long axis to form indented spheroids, instead of rings, in a fission-independent manner. *Sci. Rep.* **8**, 350 (2018).

46. Eustaquio, T. *et al.* Electron microscopy techniques employed to explore mitochondrial defects in the developing rat brain following ketamine treatment. *Exp. Cell Res.* **373**, 164–170 (2018).

47. Bosch, M. *et al.* Mammalian lipid droplets are innate immune hubs integrating cell metabolism and host defense. *Science* **370**, eaay8085 (2020).

48. Samrat, S. K., Ha, B. L., Zheng, Y. & Gu, H. Characterization of Elements Regulating the Nuclear-to-Cytoplasmic Translocation of ICP0 in Late Herpes Simplex Virus 1 Infection. *J. Virol.* **92**, (2018).

49. Lopez, P., Van Sant, C. & Roizman, B. Requirements for the Nuclear-Cytoplasmic Translocation of Infected-Cell Protein 0 of Herpes Simplex Virus 1. *J. Virol.* **75**, 3832–3840 (2001).

50. Lengyel, J., Strain, A. K., Perkins, K. D. & Rice, S. A. ICP27-dependent resistance of herpes simplex virus type 1 to leptomycin B is associated with enhanced nuclear localization of ICP4 and ICP0. *Virology* **352**, 368–379 (2006).

51. Cai, M. *et al.* Identification of the molecular determinants for nuclear import of PRV EP0. *Biol. Chem.* **400**, 1385–1394 (2019).

52. Pasdeloup, D., Labetoulle, M. & Rixon, F. J. Differing Effects of Herpes Simplex Virus 1 and Pseudorabies Virus Infections on Centrosomal Function. *J. Virol.* **87**, 7102–7112 (2013).

53. Avitabile, E. *et al.* Redistribution of microtubules and Golgi apparatus in herpes simplex virus-infected cells and their role in viral exocytosis. *J. Virol.* **69**, 7472–7482 (1995).

54. Vyas, N. *et al.* Cryo-Structured Illumination Microscopic Data Collection from Cryogenically Preserved Cells. *J. Vis. Exp.* 62274 (2021) doi:10.3791/62274.

55. Sukhorukov, V. M., Dikov, D., Reichert, A. S. & Meyer-Hermann, M. Emergence of the Mitochondrial Reticulum from Fission and Fusion Dynamics. *PLoS Comput. Biol.* **8**, e1002745 (2012).

56. Youle, R. J. & van der Bliek, A. M. Mitochondrial Fission, Fusion, and Stress. *Science* **337**, 1062–1065 (2012).

57. Bartolák-Suki, E., Imsirovic, J., Nishibori, Y., Krishnan, R. & Suki, B. Regulation of Mitochondrial Structure and Dynamics by the Cytoskeleton and Mechanical Factors. *Int. J. Mol. Sci.* **18**, 1812 (2017).

58. Bowes, T. & Gupta, R. S. Novel mitochondrial extensions provide evidence for a link between microtubule-directed movement and mitochondrial fission. *Biochem. Biophys. Res. Commun.* **376**, 40–45 (2008).

59. Silva Ramos, E., Larsson, N.-G. & Mourier, A. Bioenergetic roles of mitochondrial fusion. *Biochim. Biophys. Acta BBA - Bioenerg.* **1857**, 1277–1283 (2016).

60. Liu, X. & Hajnóczky, G. Altered fusion dynamics underlie unique morphological changes in mitochondria during hypoxia–reoxygenation stress. *Cell Death Differ.* **18**, 1561–1572 (2011).

61. Li, J. *et al.* Mitochondrial elongation-mediated glucose metabolism reprogramming is essential for tumour cell survival during energy stress. *Oncogene* **36**, 4901–4912 (2017).

62. Combs, J. A. *et al.* Human Cytomegalovirus Alters Host Cell Mitochondrial Function during Acute Infection. *J. Virol.* **94**, (2020).

63. Li, Y., Boehning, D. F., Qian, T., Popov, V. L. & Weinman, S. A. Hepatitis C virus core protein increases mitochondrial ROS production by stimulation of $Ca2+$ uniporter activity. *FASEB J.* **21**, 2474–2485 (2007).

64. Muraro, S. P. *et al.* Respiratory Syncytial Virus induces the classical ROS-dependent NETosis through PAD-4 and necroptosis pathways activation. *Sci. Rep.* **8**, 14166 (2018).

65. Lassoued, S. *et al.* Epstein-Barr virus induces an oxidative stress during the early stages of infection in B lymphocytes, epithelial, and lymphoblastoid cell lines. *Mol. Cell. Biochem.* **313**, 179–186 (2008).

66. Tanaka, M., Sata, T. & Kawaguchi, Y. The product of the Herpes simplex virus 1 UL7 gene interacts with a mitochondrial protein, adenine nucleotide translocator 2. *Virol. J.* **5**, 125 (2008).

67. Derakhshan, M., Willcocks, M. M., Salako, M. A., Kass, G. E. N. & Carter, M. J. Human herpesvirus 1 protein US3 induces an inhibition of mitochondrial electron transport. *J. Gen. Virol.* **87**, 2155–2159 (2006).

68. Saffran, H. A., Pare, J. M., Corcoran, J. A., Weller, S. K. & Smiley, J. R. Herpes simplex virus eliminates host mitochondrial DNA. *EMBO Rep.* **8**, 188–193 (2007).

69. Chadha, P. *et al.* Domain Interaction Studies of Herpes Simplex Virus 1 Tegument Protein UL16 Reveal Its Interaction with Mitochondria. *J. Virol.* **91**, e01995-16 (2017).

811   70. McSharry, B. P., Jones, C. J., Skinner, J. W., Kipling, D. & Wilkinson, G. W. G. Human telomerase
812   reverse transcriptase-immortalized MRC-5 and HCA2 human fibroblasts are fully permissive for
813   human cytomegalovirus. *J. Gen. Virol.* **82**, 855–863 (2001).

814   71. Albecka, A. *et al.* Dual Function of the pUL7-pUL51 Tegument Protein Complex in Herpes Simplex
815   Virus 1 Infection. *J. Virol.* **91**, (2017).

816   72. Schindelin, J. *et al.* Fiji: an open-source platform for biological-image analysis. *Nat. Methods* **9**,
817   676–682 (2012).

818   73. Kenny, M. & Schoen, I. Violin SuperPlots: visualizing replicate heterogeneity in large data sets.
819   *Mol. Biol. Cell* **32**, 1333–1334 (2021).

820   74. Gómez-Rubio, V. ggplot2 - Elegant Graphics for Data Analysis (2nd Edition). *J. Stat. Softw.* **77**,
821   (2017).

822   75. Racine, J. S. RStudio: A Platform-Independent IDE for R and Sweave: Software Review. *J. Appl.*
823   *Econom.* **27**, 167–172 (2012).

824   76. Lord, S. J., Velle, K. B., Mullins, R. D. & Fritz-Laylin, L. K. SuperPlots: Communicating
825   reproducibility and variability in cell biology. *J. Cell Biol.* **219**, e202001064 (2020).

826   77. Shafaq-Zadah, M., Dransart, E. & Johannes, L. Clathrin-independent endocytosis, retrograde
827   trafficking, and cell polarity. *Curr. Opin. Cell Biol.* **65**, 112–121 (2020).

828